

See discussions, stats, and author profiles for this publication at: <https://www.researchgate.net/publication/322970639>

# Anisotropy of Observed and Simulated Turbulence in Marine Stratocumulus

Article in *Journal of Advances in Modeling Earth Systems* · February 2018

DOI: 10.1002/2017MS001140

CITATIONS

4

READS

124

4 authors:



Jesper Grønnegaard Pedersen  
University of Warsaw

11 PUBLICATIONS 47 CITATIONS

[SEE PROFILE](#)



Yongfeng Ma  
University of Warsaw

15 PUBLICATIONS 87 CITATIONS

[SEE PROFILE](#)



Wojciech W. Grabowski  
National Center for Atmospheric Research

210 PUBLICATIONS 7,300 CITATIONS

[SEE PROFILE](#)



Szymon P. Malinowski  
University of Warsaw

163 PUBLICATIONS 1,583 CITATIONS

[SEE PROFILE](#)

Some of the authors of this publication are also working on these related projects:



Cloud Microdynamics [View project](#)



"Cloud-MicroPhysics-Turbulence-Telemetry" (COMPLETE) [View project](#)

## RESEARCH ARTICLE

10.1002/2017MS001140

## Key Points:

- Typical-resolution LES of the stratocumulus-topped boundary layer captures observed anisotropy of below-cloud-top turbulence reasonably well
- Decreasing the horizontal grid spacing and/or increasing the SGS mixing length leads to increased dominance of vertical fluctuations
- Performed simulations indicate concurrence of increased dominance of vertical fluctuations and increased entrainment velocity/decreased LWP

## Supporting Information:

- Supporting Information S1

## Correspondence to:

J. G. Pedersen,  
jesper@igf.fuw.edu.pl

## Citation:

Pedersen, J. G., Ma, Y.-F., Grabowski, W. W., & Malinowski, S. P. (2018). Anisotropy of observed and simulated turbulence in marine stratocumulus. *Journal of Advances in Modeling Earth Systems*, 10, 500–515. <https://doi.org/10.1002/2017MS001140>

Received 4 AUG 2017

Accepted 1 FEB 2018

Accepted article online 6 FEB 2018

Published online 23 FEB 2018

© 2018. The Authors.

This is an open access article under the terms of the Creative Commons Attribution-NonCommercial-NoDerivs License, which permits use and distribution in any medium, provided the original work is properly cited, the use is non-commercial and no modifications or adaptations are made.

## Anisotropy of Observed and Simulated Turbulence in Marine Stratocumulus

J. G. Pedersen<sup>1</sup>, Y.-F. Ma<sup>1</sup>, W. W. Grabowski<sup>1,2</sup>, and S. P. Malinowski<sup>1</sup>
<sup>1</sup>Faculty of Physics, Institute of Geophysics, University of Warsaw, Warsaw, Poland, <sup>2</sup>National Center for Atmospheric Research, Boulder, Colorado, USA

**Abstract** Anisotropy of turbulence near the top of the stratocumulus-topped boundary layer (STBL) is studied using large-eddy simulation (LES) and measurements from the POST and DYCOMS-II field campaigns. Focusing on turbulence  $\sim 100$  m below the cloud top, we see remarkable similarity between day-time and nocturnal flight data covering different inversion strengths and free-tropospheric conditions. With  $\lambda$  denoting wavelength and  $z_t$  cloud-top height, we find that turbulence at  $\lambda/z_t \simeq 0.01$  is weakly dominated by horizontal fluctuations, while turbulence at  $\lambda/z_t > 1$  becomes strongly dominated by horizontal fluctuations. Between are scales at which vertical fluctuations dominate. Typical-resolution LES of the STBL (based on POST flight 13 and DYCOMS-II flight 1) captures observed characteristics of below-cloud-top turbulence reasonably well. However, using a fixed vertical grid spacing of 5 m, decreasing the horizontal grid spacing and increasing the subgrid-scale mixing length leads to increased dominance of vertical fluctuations, increased entrainment velocity, and decreased liquid water path. Our analysis supports the notion that entrainment parameterizations (e.g., in climate models) could potentially be improved by accounting more accurately for anisotropic deformation of turbulence in the cloud-top region. While LES has the potential to facilitate improved understanding of anisotropic cloud-top turbulence, sensitivity to grid spacing, grid-box aspect ratio, and subgrid-scale model needs to be addressed.

## 1. Introduction

As recently reported by Mellado (2017), laboratory and numerical experiments have in combination with field measurements over the last few decades greatly improved our understanding of entrainment of free-tropospheric air into the stratocumulus-topped boundary layer (STBL). Nevertheless, important questions still remain open, e.g., regarding the influence of radiative and evaporative cooling, turbulence, large-scale flow structures, microphysics, and in particular interactions between these phenomena (see Mellado, 2017; Wood, 2012). This lack of sufficient knowledge adds to the significant uncertainties and biases in representation of stratocumulus clouds seen in current climate models (e.g., Noda & Satoh, 2014). Based on the analysis of measurements from the Physics Of Stratocumulus Top (POST) field campaign (Gerber et al., 2010, 2013), Jen-La Plante et al. (2016) hypothesize that deficiencies of existing entrainment parameterizations are partly due to poor understanding of turbulence in the stably stratified inversion layer capping the STBL. The general topic of stratified turbulence is, however, the focus of ongoing research, and progress is being made (e.g., Khani & Waite, 2015; Lindborg, 2006; Riley & Lelong, 2000; Waite, 2011). The present study is specifically aimed at improved understanding of turbulence in the cloud-top region of the STBL and the impact of the capping inversion.

Following Malinowski et al. (2013), we divide the entrainment interfacial layer (EIL; Caughey et al., 1982) separating the free troposphere (FT) from the well-mixed cloud-top layer (CTL) into two regions: the turbulent inversion sublayer (TISL) characterized by a low cloud condensate mixing ratio, and below that, the more moist cloud-top mixing sublayer (CTMSL). An example of this layer division based on results from a large-eddy simulation is shown in Figure 1. Details of the simulation setup are given in section 3. Jen-La Plante et al. (2016) find, based on the POST data, that the Ozmidov and Corrsin scales ( $L_O$  and  $L_C$ ; see, e.g., Smyth & Moum, 2000) are around 0.5 m in the TISL and 3 m in the CTMSL. The two length scales, defined as  $L_O = (\epsilon/N^3)^{1/2}$  and  $L_C = (\epsilon/S^3)^{1/2}$  with  $\epsilon$ ,  $N$ , and  $S$  representing the dissipation rate of turbulent kinetic energy, mean Brunt-Väisälä frequency, and mean wind shear, indicate the sizes of the smallest turbulent eddies

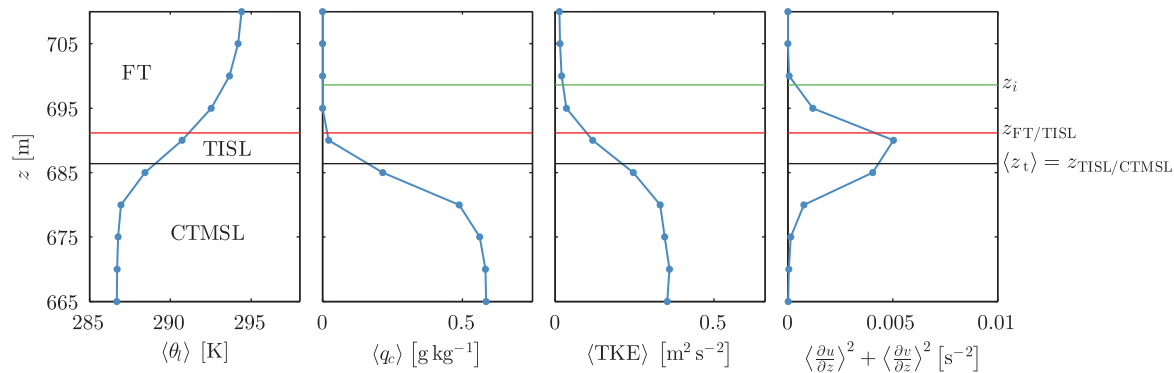


**Figure 1.** Vertical profiles of domain-averaged liquid water potential temperature, cloud condensate mixing ratio, turbulent kinetic energy, and wind shear at the time  $t = 340$  min in simulation  $P_{10.5}$  (see section 3 for details). The red line marks the boundary between the FT and the TISL ( $z_{FT/TISL}$ , defined as the highest altitude with  $\frac{\partial \langle \theta_l \rangle}{\partial z} > 0.2 \text{ K m}^{-1}$  and  $\langle TKE \rangle > 0.1 \text{ m}^2 \text{ s}^{-2}$ ), and the black line the boundary between the TISL and the CTMSL ( $z_{TISL/CTMSL}$ , defined as the average height of  $q_c = 0.05 \text{ g kg}^{-1}$  and coinciding with the domain-averaged cloud-top height  $\langle z_t \rangle$ ). The green line ( $z_i$ ) marks the highest altitude of  $\frac{\partial \langle \theta_l \rangle}{\partial z} = 0.2 \text{ K m}^{-1}$ .

deformed by stable stratification and wind shear, i.e., eddies larger than  $L_O$  and  $L_C$  tend to be vertically suppressed and horizontally stretched. Considering the small values of  $L_O$  and  $L_C$  observed in the cloud-top region, Jen-La Plante et al. (2016) suggest that entrainment parameterizations should be revisited with such anisotropic deformation in mind.

Large-eddy simulation (LES) is generally considered a valuable tool for studying the STBL (e.g., Stevens et al., 2005), especially in combination with measurements, and we believe it has the potential to help us understand more accurately the role of anisotropic turbulence in the entrainment processes. The method, however, still suffers from sensitivities to subgrid-scale (SGS) modeling, numerics, resolution, and domain size (see, e.g., Cheng et al., 2010; Guo et al., 2008; Matheou & Chung, 2014; Nishizawa et al., 2015; Pedersen et al., 2016; Pressel et al., 2017; Yamaguchi et al., 2013; Yamaguchi & Randall, 2012), and it should be used with these deficiencies in mind. Here we look at how well anisotropy of cloud-top turbulence across a range of scales is represented in conventional and implicit LES of the STBL. We use grid spacing typical for current LES studies, and we explore how inaccurate representation of cloud-top turbulence may affect evolution of the simulated cloud. Our analysis is focused on simulations based on data from flight 13 of the POST campaign and flight 1 of the second Dynamics and Chemistry of Marine Stratocumulus campaign (DYCOMS-II, Stevens et al., 2003a). Henceforth, we refer to these two cases as P13 and D1. Using the terminology of Gerber et al. (2010) and Malinowski et al. (2013), D1 is a classical stratocumulus case characterized by a shallow and strong inversion capped by a stable and dry free troposphere. It has been the subject of several LES studies, including Stevens et al. (2005), Kurowski et al. (2009), Yamaguchi and Randall (2012), and Pedersen et al. (2016). The P13 case, on the other hand, is considered as a nonclassical case. It is investigated in detail by Malinowski et al. (2013) and was used as the basis for the LES study by Kopec et al. (2016) on the influence of wind shear and radiative cooling on the STBL. The distinction between classical and nonclassical STBLs is not based on rigid criteria but is rather a subjective assessment. In D1, the liquid water potential temperature  $\theta_l$  increases from  $\sim 290$  to  $\sim 298 \text{ K}$  over a  $\sim 10 \text{ m}$  thick layer in the cloud-top region while the total water mixing ratio  $q_t$  decreases from  $\sim 9$  to  $\sim 1.5 \text{ g kg}^{-1}$ . In P13, the inversion is weaker;  $\theta_l$  increases from  $\sim 286$  to  $\sim 292 \text{ K}$  over a  $\sim 30 \text{ m}$  thick layer. It is, however, mainly the lack of a sharp decrease in  $q_t$  above the cloud which makes P13 a nonclassical case (see, e.g., Malinowski et al., 2013, Figure 3). The FT is not significantly drier than the STBL.

The present study is an extension of Pedersen et al. (2016), who show that the evolution of the cloud in implicit LES (ILES) of the D1 case is sensitive to changes in the applied horizontal grid spacing ( $\Delta x$  and  $\Delta y$ ) at vertical grid spacings ( $\Delta z$ ) of 5, 10, and 15 m. The observed sensitivity is attributed to anisotropy of the simulated turbulence found to depend on the grid-box aspect ratio ( $\Delta x/\Delta z$  and  $\Delta y/\Delta z$ ). In the present study, we focus on simulations with a vertical grid spacing of 5 m which is typical for LES of the STBL (see, e.g., Kurowski et al., 2009; Stevens et al., 2005). The horizontal grid spacing is varied between 5, 10, and 30 m, which are also typical values. In simulation of the P13 case, Kopec et al. (2016) use a grid-box size of  $\Delta x \times \Delta y \times \Delta z = 20 \times 20 \times 2.5 \text{ m}^3$ , and to our knowledge, the shortest grid spacing used to date in LES of the

D1 case is 2.5 m in both the horizontal and vertical directions (Matheou & Chung, 2014). However, even with a resolution this fine, grid dependency is still observed, e.g., as the grid spacing is increased from 2.5 to 5 m. Whether the solution has fully converged at the 2.5 m grid spacing remains an open question (see also Yamaguchi and Randall (2012) who compare D1 simulations with grid-box sizes of  $5 \times 5 \times 2.5$  and  $10 \times 10 \times 2.5$  m<sup>3</sup>). Recently Sullivan et al. (2016) simulated a stably stratified 100 m deep boundary layer using a grid spacing of 0.39 m, but in a domain of only 400 m<sup>3</sup>. Simulation of the full STBL with a depth of  $\sim 1$  km using a horizontal/vertical grid spacing significantly shorter than  $\sim 2.5$  m is not yet feasible in terms of computational resources. As a way to reduce uncertainty of existing scaling laws describing cloud-top entrainment, Mellado (2017) proposes to combine direct numerical simulation (DNS) at centimeter-scale resolution focused on the cloud-top region (e.g., Mellado, 2010) with LES of the entire STBL at meter-scale resolution. The present study will in itself shed light on the role of turbulence anisotropy in the cloud-top region, but we also expect it to be helpful in setting up future simulations combining LES and DNS. We focus on how changes in horizontal resolution and modeling of SGS fluxes affect the anisotropic deformation of simulated turbulence and cloud evolution. Observations are used as rough validation of the performed simulations and as a framework for putting intersimulation differences into perspective. Due to the idealized nature of the simulations, we do not expect perfect agreement with the observations.

The paper is structured as follows. In sections 2 and 3, we briefly introduce the measurements used in the study and the applied model, and in section 4, we present the results of our analysis; first regarding measurements and second regarding simulations. In section 5, we discuss and summarize our findings.

## 2. Measurements

The two measuring campaigns considered here (POST and DYCOMS-II) took place off the coast of California in 2008 and 2001. Both campaigns aimed at improved understanding of entrainment at the top of the STBL. Information about instrumentation, flight patterns, etc. can be found in Gerber et al. (2013) and Stevens et al. (2003a). See also [www.eol.ucar.edu/field\\_projects/post](http://www.eol.ucar.edu/field_projects/post) and [www.eol.ucar.edu/field\\_projects/dycoms-ii](http://www.eol.ucar.edu/field_projects/dycoms-ii). Here we focus on data from DYCOMS-II flight 1 (D1) and POST flight 13 (P13) which both are nocturnal flights. The other flights included in this study are POST flights 3 (nocturnal/nonclassical), 5 (nocturnal/nonclassical), 10 (daytime/classical), 12 (nocturnal/classical), and 14 (nocturnal/nonclassical). The division between classical and nonclassical STBL cases follows Malinowski et al. (2013) and Gerber et al. (2010).

## 3. Model Setup

The simulations presented here are performed in an Eulerian anelastic framework using the EULAG model (Prusa et al., 2008), and we perform both conventional LES and ILES (see section 3.1). The model is set up to solve for the three velocity components  $u$ ,  $v$ , and  $w$  in the  $x$ -direction,  $y$ -direction, and  $z$ -direction, the potential temperature  $\theta$ , and mixing ratios of cloud condensate  $q_c$  and water vapor  $q_w$ . Precipitation is excluded. Potential temperature and velocity components are advected using the “infinite-gauge” variant of the Multi-dimensional Positive Definite Advection Transport Algorithm (MPDATA; Smolarkiewicz, 2006), while all other variables are advected using the basic variant of the algorithm. Modeling of condensation/evaporation is based on an assumption of no supersaturation, following Grabowski and Smolarkiewicz (1990, 2002). The flow is periodic across the lateral boundaries of the computational domain, i.e., in the  $x$ -direction and  $y$ -direction, and the upper boundary is impermeable with free-slip conditions. The lower boundary is impermeable with partial-slip conditions imposed through near-surface momentum fluxes.

These are given by:

$$\tau_{uw}(z) = -C_d |\mathbf{u}_0| u_0 e^{-z/h_d} \quad (1)$$

$$\tau_{vw}(z) = -C_d |\mathbf{u}_0| v_0 e^{-z/h_d} \quad (2)$$

where  $|\mathbf{u}| = \sqrt{u^2 + v^2}$  is the wind speed and  $C_d$  is a drag coefficient. Subscript 0 refers to surface values. In both cases (P13 and D1), we set  $C_d = 0.001$  and the surface air density of the idealized anelastic base state  $\bar{\rho}_0$  (Clark & Farley, 1984) to  $1.2 \text{ kg m}^{-3}$ . To get realistic results with ILES, we find it necessary to specify an attenuation length scale  $h_d$  on the order of a few  $\Delta z$  (see also Margolin et al., 1999; Piotrowski et al., 2009).

**Table 1**

Values Used in Simulations Based on POST Flight 13 and DYCOMS-II Flight 1<sup>a</sup>

	$H_0$ (W m <sup>-2</sup> )	$Q_0$ (W m <sup>-2</sup> )	$w_s$ (m s <sup>-1</sup> )	$P_0$ (hPa)	$U_g$ (m s <sup>-1</sup> )	$V_g$ (m s <sup>-1</sup> )
P13	5	10	$3.0 \times 10^{-6} z$	1014.7	5.0	-7.0
D1	15	115	0	1017.8	7.0	-5.5

<sup>a</sup>Sensible and latent surface heat fluxes, large-scale subsidence velocity, surface air pressure, and components of the geostrophic wind.

Distributing the applied surface fluxes over a few grid points in the vertical ensures a linear height-dependency of the total fluxes (applied plus resolved) near the surface. We use  $h_d = 50$  m but note that our results are not very sensitive to the exact value of this parameter. In conventional LES, we set  $1/h_d = 0$ . Near-surface fluxes of sensible and latent heat are given by:

$$h(z) = (c_p \bar{\rho}_0)^{-1} H_0 e^{-z/h_d} \quad (3)$$

$$q(z) = (L_v \bar{\rho}_0)^{-1} Q_0 e^{-z/h_d}. \quad (4)$$

Applied values of  $H_0$  and  $Q_0$  are given in Table 1 along with the large-scale subsidence velocity  $w_s$ , surface air pressure  $P_0$ , and geostrophic wind components  $U_g$  and  $V_g$  representing a large-scale horizontal pressure gradient. The latent heat of condensation  $L_v$  is set to  $2.47 \times 10^6$  J kg<sup>-1</sup>, and the specific heat at constant pressure  $c_p$  to  $1015$  J kg<sup>-1</sup> K<sup>-1</sup>. In both sets of simulations,  $U_g$  and  $V_g$  are constant with height, and the Coriolis parameter is set to  $7.3 \times 10^{-5}$  s<sup>-1</sup> which corresponds to a latitude of 30°.

We perform simulations with  $\Delta_{xy} = \Delta x = \Delta y = \{5, 10, 30\}$  and  $\Delta z = 5$  m. The time step  $\Delta t$  is chosen such that the maximum value of  $\text{CFL} = \Delta t \left( \frac{u}{\Delta x} + \frac{v}{\Delta y} + \frac{w}{\Delta z} \right)$  throughout the domain and simulation period is  $\sim 0.5$ . An overview of the performed simulations is given in Table 2. Simulations based on P13/D1 are denoted by P/D followed by  $\Delta_{xy}$  and  $\Delta z$ . Side lengths of the computational domain in the x-direction, y-direction, and z-direction are given by  $L_x$ ,  $L_y$ , and  $L_z$ .

### 3.1. Subgrid-Scale Model

The performed simulations include both conventional LES and ILES. In conventional LES, we follow Sorbjan (1996) and calculate the SGS momentum fluxes based on an eddy viscosity given by

$$K_m = c_m \Lambda E^{1/2} \quad (5)$$

where  $E$  is the SGS turbulent kinetic energy (TKE) determined through its own prognostic equation (Deardorff, 1980), and  $c_m$  is a constant of 0.0856. SGS fluxes of  $\theta$ ,  $q_c$ , and  $q_v$  are calculated based on the eddy diffusivities

**Table 2**

Overview of Performed Simulations<sup>a</sup>

Simulation	$\Delta_{xy}$ (m)	$\Delta z$ (m)	$\Delta t$ (s)	$\Delta$	$L_x = L_y$ (km)	$L_z$ (km)
P <sub>30,5</sub>	30	5	0.4		3.0	1.2
P <sub>10,5</sub>	10	5	0.2		3.0	1.2
P <sub>5,5</sub>	5	5	0.1		3.0	1.2
P <sub>30,5,<math>\Delta z</math></sub>	30	5	0.4	$\Delta z$	3.0	1.2
P <sub>30,5,<math>\Delta xyz</math></sub>	30	5	0.4	$(\Delta x \Delta y \Delta z)^{1/3}$	3.0	1.2
P <sub>30,5,<math>\Delta x</math></sub>	30	5	0.4	$\Delta x$	3.0	1.2
D <sub>30,5</sub>	30	5	0.4		4.2	1.5
D <sub>10,5</sub>	10	5	0.2		4.2	1.5
D <sub>30,5,<math>\Delta xyz</math></sub>	30	5	0.4	$(\Delta x \Delta y \Delta z)^{1/3}$	4.2	1.5

<sup>a</sup>Horizontal and vertical grid spacing, time step length, mixing length used in the subgrid-scale model, and horizontal and vertical extents of the computational domain.

**Table 3**  
Initial Conditions for P13 Simulations<sup>a</sup>

$z$	(m)	0	180	560	595	1,000	1,200
$\theta_l$	(K)	286.1	286.1	286.1	291.8	299.8	299.8
$q_t$	(g kg <sup>-1</sup> )	9.21	9.21	8.77	7.71	2.53	2.53

<sup>a</sup>Values defining the piecewise linear and horizontally homogeneous initial conditions used in simulations based on P13.

$$K_h = K_{q_c} = K_{q_v} = K_m / \text{Pr} \quad (6)$$

where Pr is the Prandtl number set to 0.42. The length scale  $\Lambda$  is given by  $\min[\Delta, c_L z]$  where  $c_L$  is a constant set to 0.845. Typically  $\Delta = (\Delta x \Delta y \Delta z)^{1/3}$ , but for very anisotropic grid boxes (e.g., with  $\Delta x = \Delta y$  much larger than  $\Delta z$ ) this is not an obvious choice (Scotti et al., 1993). To explore the impact of changing  $\Delta$ , we perform simulations with  $\Delta = \{\Delta z, (\Delta x \Delta y \Delta z)^{1/3}, \Delta x\}$  as indicated in Table 2 (similar investigations were done by Kurowski et al. (2014) regarding deep moist convection and by Nishizawa et al. (2015) regarding the dry atmospheric boundary layer).

In ILES, the SGS model is switched off. This is equivalent to setting  $\Delta = 0$  and relying solely on truncation terms of the applied numerical scheme to account for the effects of unresolved turbulence. The MPDATA scheme used here, has been shown by Grinstein et al. (2007) and Margolin and Rider (2002) to be well suited for ILES (see also Grabowski, 2014; Pedersen et al., 2016). Our choice to use ILES is motivated by Stevens et al. (2005), Piotrowski et al. (2009), Kurowski et al. (2009), and Pressel et al. (2017) who find ILES to perform better than conventional LES.

### 3.2. POST Flight 13 Simulation Setup

In the P13 simulations, longwave radiative fluxes are given by

$$F_{\text{rad}} = \begin{cases} (c_p \bar{\rho})^{-1} (F_0 e^{-\int_z^\infty k q_c dz}) & \text{for } z < z_t \\ (c_p \bar{\rho})^{-1} (F_0 e^{-\int_z^\infty k q_c dz} + C(z - z_t)^{1/2}) & \text{for } z \geq z_t, \end{cases} \quad (7)$$

with  $F_0 = 80 \text{ W m}^{-2}$ ,  $k = 800 \text{ m}^{-1}$ ,  $C = 0.5 \text{ W m}^{-5/2}$  (following Kopec et al., 2016). The local cloud-top height  $z_t$  is defined as the maximum altitude in each column at which  $q_c$  interpolates to  $0.05 \text{ g kg}^{-1}$  (corresponding to 9% of the initial maximum value of  $q_c$  which is  $0.57 \text{ g kg}^{-1}$ ). Initial profiles of  $\theta_l$  and  $q_t = q_c + q_v$  are piecewise linear functions defined by the values given in Table 3. Initially we set  $u = U_g$  and  $v = V_g$  at all heights. The P13 simulations are run for 360 min, and data are stored every 20 min.

### 3.3. DYCOMS-II Flight 1 Simulation Setup

In the D1 simulations, longwave radiative fluxes are given by

$$F_{\text{rad}} = (c_p \bar{\rho})^{-1} \left( F_0 e^{-Q(z, \infty)} + F_1 e^{-Q(0, z)} \right) \quad (8)$$

where

$$Q(a, b) = \kappa \int_a^b \bar{\rho} q_c dz \quad (9)$$

and  $F_0 = 70 \text{ W m}^{-2}$ ,  $F_1 = 22 \text{ W m}^{-2}$ , and  $\kappa = 85 \text{ m}^2 \text{ kg}^{-1}$  (following Stevens et al., 2005). To avoid situations with strong dissolution of the simulated cloud and cloud cover fractions much smaller than 1, we choose, in contrast to the setup of Stevens et al. (2005), not to apply any large-scale subsidence. This choice follows from the results of the D1 EULAG simulation presented by Kurowski et al. (2009), who after 4 h of simulation time with large-scale subsidence included (following Stevens et al., 2005), find that the domain-averaged liquid water path (LWP) is reduced to  $\sim 20 \text{ g m}^{-2}$  and the cloud cover fraction to  $\sim 0.5$  (i.e., values quite far from the observation-based estimates of  $\sim 60 \text{ g m}^{-2}$  and  $\sim 1$ ). We find that setting  $w_s = 0$  prevents such severe cloud thinning, and in the setup of the D1 simulations presented here, we prioritize to maintain a high cloud cover fraction and LWP-values in reasonable agreement with observations over including large-



scale subsidence. We furthermore note that the large-scale subsidence velocity is not easily measured, and that the value of  $w_s = 3.75 \times 10^{-6} z \text{ m s}^{-1}$  used by Stevens et al. (2005) appears to be a quite crude estimate.

Regarding initial conditions, we follow Stevens et al. (2005) and use:

$$\theta_l = \begin{cases} 289.0 \text{ K} & \text{for } z \leq z_i \\ 297.5 + (z - z_i)^{1/3} \text{ K} & \text{for } z > z_i \end{cases} \quad (10)$$

$$q_t = \begin{cases} 9.0 \text{ g kg}^{-1} & \text{for } z \leq z_i \\ 1.5 \text{ g kg}^{-1} & \text{for } z > z_i \end{cases} \quad (11)$$

with  $z_i = 840 \text{ m}$ . As in the P13-simulations, we initially set  $u = U_g$  and  $v = V_g$  at all heights, and define the cloud top based on a threshold value of  $0.05 \text{ g kg}^{-1}$  (corresponding to 11% of the initial maximum value of  $q_c$  which is  $0.45 \text{ g kg}^{-1}$ ). Simulations  $D_{30,5}$  and  $D_{30,5,\Delta xyz}$  are run for 460 min. To reduce computational time and to minimize the influence of spin-up effects, simulation  $D_{10,5}$  is initialized with fields obtained from  $D_{30,5}$  at  $t = 240 \text{ min}$  interpolated to  $10 \text{ m}$  horizontal grid spacing. After initialization  $D_{10,5}$  is run for 220 min. Data are stored every 20 min.

## 4. Results

After a brief discussion of observations from D1 and several POST flights, we turn our attention to results of the performed simulations; first we investigate how grid spacing and SGS mixing length affect the anisotropy of simulated turbulence, and second we look at associated effects on the evolution of the simulated cloud. As a measure of anisotropy of observed and simulated turbulence, we define the ratio

$$R = \frac{E_u + E_v}{2E_w} \quad (12)$$

where  $E_u$ ,  $E_v$ , and  $E_w$  represent spectral energy densities of  $u$ ,  $v$ , and  $w$ . Values of  $R$  close to 1 indicate isotropic turbulence, while  $R > 1$  and  $R < 1$  indicate anisotropic turbulence dominated by horizontal and vertical fluctuations, respectively. A similar measure is used by Mauritsen and Svensson (2007) but their definition is based on the total variances of  $u$ ,  $v$ , and  $w$  rather than on the spectral energy densities. With the method used here, we obtain a scale-dependent measure of the anisotropy, which we believe to be advantageous in the study of entrainment. Based on DNS, de Lozar and Mellado (2013) suggest that only eddies smaller than  $\sim 60 \text{ m}$  take part in the entrainment process. Anisotropy specific to these small scales is unlikely to be reflected clearly in an anisotropy measure based on total variances.

### 4.1. Measurements

Figure 2 shows  $R$  as a function of the wavelength  $\lambda$  normalized by the cloud-top altitude ( $z_{t,avg}$ ). In addition to observations from P13 (black circles) and D1 (red squares), we also show observations from POST flights 3, 5, 10, 12, and 14.  $R$  is calculated through 1-D Fourier transformation of  $u$ ,  $v$ , and  $w$  recorded along the flight paths. Using Taylor's hypothesis, the measured time series are converted into spatial records (assuming a constant speed of the aircraft). Error bars indicate  $\pm$  the standard deviation of  $R$  in each  $\lambda$ -bin. To avoid an overly cluttered figure these have only been added to every other data point from P13 and D1. The shown  $R$ -values are from periods in which the instrumented aircraft flew horizontally near the cloud top; typically  $\sim 100 \text{ m}$  below it. For an example of a POST flight pattern (flight 3), see Figure 1 in Jen-La Plante et al. (2016); flight 3 includes two horizontal segments starting at  $t \simeq 0.85 \times 10^4 \text{ s}$  and at  $t \simeq 1.25 \times 10^4 \text{ s}$ . Averaged altitudes of the used measurements ( $\pm$  the standard deviation for the POST flights) are given as  $z_{t,\div}$  in Table 4 which also includes values of  $z_{t,avg}$  and the cloud-base altitude  $z_{b,avg}$ . The values of  $z_{t,avg}$  and  $z_{b,avg}$  from POST are averages over the entire period of each flight ( $\pm$  the standard deviation) and indicate the highest/lowest altitudes with a liquid water content (LWC) of  $0.05 \text{ g kg}^{-1}$ . The values for D1 are based on Stevens et al. (2003b). In the legend of Figure 2, we also provide, for each flight, estimates of the entrainment velocity  $w_e$  taken from Gerber et al. (2013) and Stevens et al. (2003b).

Although the seven flights represent different conditions (see Gerber et al., 2013; Jen-La Plante et al., 2016; Malinowski et al., 2013; Stevens et al., 2003a), we see clear similarities between the derived values of  $R$ . For all flights, except D1, the observed turbulence is nearly isotropic ( $0.5 < R < 2$ ) for  $\lambda/z_{t,avg}$  less than  $\sim 1$ . It is,

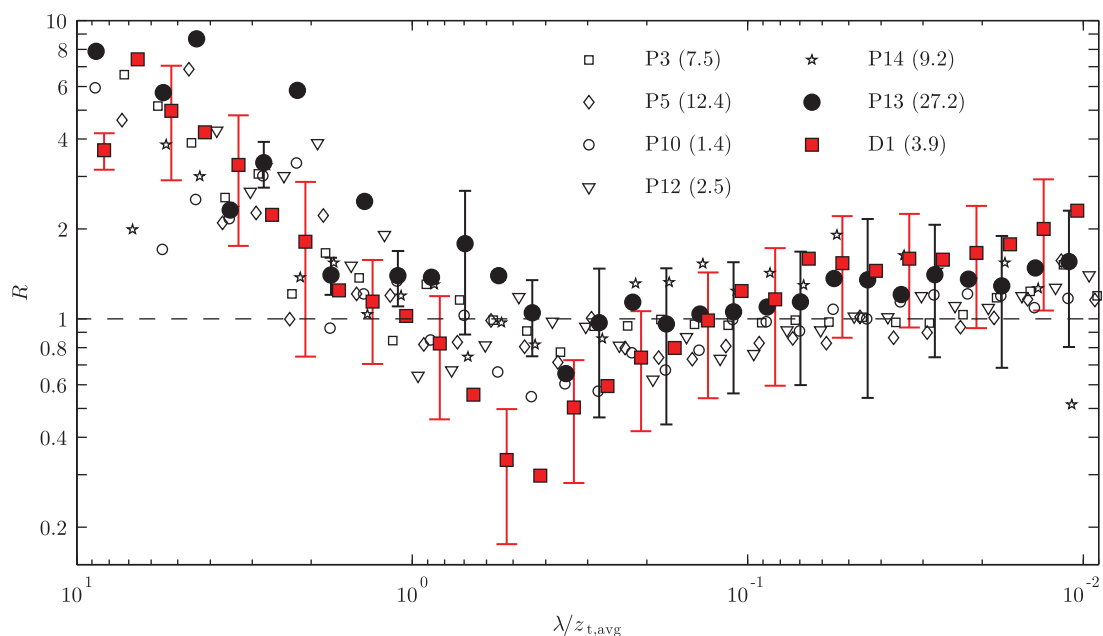


**Figure 2.** Values of  $R$  based on measurements from approximately 100 m below the cloud top. Estimates of entrainment velocities are given in the legend of the figure in units of  $\text{mm s}^{-1}$ .

however, slightly dominated by horizontal fluctuations at the smallest resolved scales ( $\lambda/z_{t,\text{avg}} \simeq 0.01$ ) and by vertical fluctuations around  $\lambda/z_{t,\text{avg}} = 0.4$ , where there is a minimum in  $R$ . Flight D1 stands out with a smaller minimum ( $R_{\text{min}} \simeq 0.3$ ) than the POST flights ( $R_{\text{min}} > 0.5$ ). At scales larger than  $\sim 0.4z_{t,\text{avg}}$ ,  $R$  increases rapidly—at similar rates in all flights—toward values of approximately 10 at  $\lambda \simeq 10z_{t,\text{avg}}$ .

It is not a surprise that the observed large-scale turbulence is anisotropic. The vertical extent ( $L_V$ ) of turbulent eddies in the STBL is generally limited by the height of the boundary layer (approximately equal to  $z_{t,\text{avg}}$ ), and eddies with a horizontal extent  $L_H \simeq 0.5\lambda > z_{t,\text{avg}}$  must therefore be anisotropic with  $L_H > L_V$ . We see this reflected in the observed anisotropy as  $R > 1$  for  $\lambda/z_{t,\text{avg}} > 2$ . From earlier studies (e.g., Agee et al., 1973; Kaimal et al., 1976; Moeng, 1986; Schmidt & Schumann, 1989; Wood & Hartmann, 2006) it is furthermore known that convectively driven large-scale motions tend to be organized in convective cells with high aspect ratios ( $L_H > L_V$ ). In the STBL, closed convective cells are seen as broad cloudy regions with positive vertical velocity, surrounded by narrow regions with reduced LWC and negative vertical velocity. Simulation results (see, e.g., de Roode et al., 2004; Kazil et al., 2017; Stevens et al., 2005; supporting information Figure S6) indicate that the width of the downdraft-dominated cell edges is equal to  $\sim z_{t,\text{avg}}$  or less, and we speculate that these regions are responsible for the observed values of  $R < 1$  at  $\lambda/z_{t,\text{avg}} \simeq 0.4$ . The smallest scales shown in Figure 2 corresponds to turbulent eddies with  $L_H$  between  $\sim 2$  and  $\sim 4$  m. We assume these eddies to be influenced across their entire extent (horizontal and vertical) by the wind shear and stratification at the measuring level of  $z_{t+}$  at which we estimate  $L_O = 3.8$  m and  $L_C = 0.6$  m based on measurements from P13. We believe these small values of  $L_O$  and  $L_C$  explain (at least in the case of P13) why the smallest eddies represented in Figure 2 are mainly dominated by horizontal fluctuations. Finally, despite the similarities in  $R$  across flights representing different STBL conditions, we see large variation in the shown estimates of

**Table 4**

Observed and Simulated Values of  $z_{t,\text{avg}}$ ,  $z_{t+}$ , and  $z_{b,\text{avg}}$ <sup>a</sup>

	Flight/ simulation	$z_{t,\text{avg}}$ (m)	$z_{t+}$ (m)	$z_{b,\text{avg}}$ (m)
Observations	P3	481 ± 17	364 ± 53	221 ± 41
	P5	473 ± 50	358 ± 48	219 ± 48
	P10	624 ± 52	575 ± 49	343 ± 57
	P12	721 ± 55	651 ± 35	407 ± 84
	P13	628 ± 36	460 ± 59	208 ± 67
	P14	509 ± 29	415 ± 29	110 ± 22
	D1	840	757	600
P13 simulations	P <sub>30,5</sub>	670	555–580	317
	P <sub>10,5</sub>	677	560–590	345
	P <sub>5,5</sub>	677	560–585	355
	P <sub>30,5,Δxyz</sub>	687	565–600	359
D1 simulations	D <sub>30,5</sub>	834	725–735	582
	D <sub>10,5</sub>	834	725–735	598
	D <sub>30,5,Δxyz</sub>	832	725–735	646

<sup>a</sup>Average altitudes of cloud top ( $z_{t,\text{avg}}$ ) and cloud base ( $z_{b,\text{avg}}$ ) in six POST flights, flight D1, and a selected subset of the performed simulations. The values of  $R$  in Figures 2, 3, and 6 are obtained at  $z = z_{t+}$ . For the simulations,  $z_{t,\text{avg}}$  and  $z_{b,\text{avg}}$  represent averages over the last 2 h of simulation time, while the values of  $z_{t+}$  indicate the interval covered over the last 2 h.



entrainment velocities. There does not seem to be a clear correlation between  $R$  and  $w_e$ . We note, however, that  $w_e$  is notoriously difficult to measure and is subject to large uncertainty.

In addition to the horizontal flight segments from which the observational data in Figure 2 is obtained, the POST campaign also included flight segments during which the aircraft flew repeatedly up and down through the EIL. From these segments of P13, we calculate mean values of  $R$  across the TISL ( $z_{\text{TISL}/\text{CTMSL}} < z < z_{\text{FT}/\text{TISL}}$ ) and across the CTMSL ( $z_{\text{CTMSL}/\text{CTL}} < z < z_{\text{TISL}/\text{CTMSL}}$ ). Here we set  $z_{\text{TISL}/\text{CTMSL}} = z_{t,\text{avg}}$ , and following Malinowski et al. (2013), we define  $z_{\text{FT}/\text{TISL}}$  as the highest altitude at which the vertical gradient of  $\theta_i$  and the TKE exceed values of  $0.2 \text{ K m}^{-1}$  and  $0.1 \text{ m}^2 \text{ s}^{-2}$ . The CTMSL/CTL interface  $z_{\text{CTMSL}/\text{CTL}}$  is defined as the height at which the square of the horizontal wind shear reaches 90% of its maximum (also following Malinowski et al., 2013). As shown by Jen-La Plante et al. (2016), the thickness of the TISL is approximately 14 m on average in P13 and the thickness of the CTMSL approximately 74 m. The porpoise-like flight segments covered shorter distances than the horizontal segments, and they only allow us to determine  $R$  at scales smaller than  $\sim 0.3z_{t,\text{avg}}$  in P13.

Considering  $0.01 \leq \lambda/z_{t,\text{avg}} \leq 0.3$  (corresponding to  $6.3 \text{ m} \leq \lambda \leq 188.4 \text{ m}$  with  $z_{t,\text{avg}} = 628 \text{ m}$ ), we find that  $R$  fluctuates between 1.0 and 3.1 in the TISL with a mean value of 1.7, between 0.9 and 1.3 in the CTMSL with a mean value of 1.1, and between 1.0 and 1.6 at  $z_{t,\pm}$  with a mean value of 1.2. The considered  $\lambda$ -range is above the estimated values of  $L_O$  and  $L_C$  in both the TISL and the CTMSL (Jen-La Plante et al. (2016) find  $(L_O, L_C) = (0.7, 0.6) \text{ m}$  in the TISL and  $(L_O, L_C) = (5.7, 3.6) \text{ m}$  in the CTMSL) as well as at  $z_{t,\pm}$ , and we expect wind shear and stable stratification to affect turbulence at these scale, acting to increase  $R$ . Radiative and evaporative cooling is on the other hand expected to decrease  $R$  by inducing vertical motion. We presume that the combined cooling effect is stronger in the CTMSL (below the cloud top) than in the TISL (above the cloud top), and that this, at least partly, explains the relatively high values of  $R$  in the TISL and the near-isotropy in the CTMSL. At  $z_{t,\pm}$  below the CTMSL, we expect the effects of cloud-top radiative and evaporative cooling to have somewhat diminished, and that this explains why the values of  $R$  at this height are slightly higher than the values in the CTMSL. Values of  $R$  obtained in the TISL are compared to simulation-based values in Figure 4 which also show values from the CTMSL.

## 4.2. Anisotropy of Simulated Turbulence

Here we compare simulated and observed turbulence in terms of the anisotropy measure  $R$  and investigate the influence of horizontal grid spacing  $\Delta_{xy}$  and SGS mixing length  $\Delta$ . First we look at results from P13 simulations and second at results from D1 simulations.

### 4.2.1. POST Flight 13 Simulations

In Figure 3a, we compare simulation-based and observation-based values of  $R$ . Black circles represent observations from P13 (as in Figure 2), and lines represent simulations based on P13. Simulated values are averages of  $R$  calculated by use of 2-D fast Fourier transformation (FFT) along the  $x$ -direction and  $y$ -direction at  $t = t_{\text{avg}} = \{240, 260, 280, 300, 320, 340, 360\} \text{ min}$ , i.e., the last 2 h of the simulation period. We note that this way of calculating  $R$  differs from the way the observation-based values are obtained. However, regarding the relatively crude comparison presented here, we are not particularly worried about this difference in calculation methods. The approach of comparing domain-averaged LES quantities to along-flight-path observations is commonly applied; see, e.g., Stevens et al. (2005) regarding cloud boundaries and vertical profiles of second and third moments of vertical velocity. As shown by Kelly and Wyngaard (2006), two-dimensional spectra differ somewhat from one-dimensional spectra (particularly as the wavenumber approaches zero), and we do also see differences between  $R$ -values based on 1-D and 2-D FFT of the simulated velocity components. However, not to a degree that would significantly change the outcome of our analysis.

The shown values of  $R$  are obtained at  $z_{t,\pm}$  which we define as the vertical grid level closest to  $\langle z_t(t) \rangle - 100 \text{ m}$ . Angular brackets  $\langle - \rangle$  denote an average across all columns of the computational domain, and  $z_t$  is the local cloud-top altitude (as in equation (7)). For the simulation results, we normalize  $\lambda$  by the average of  $\langle z_t(t) \rangle$  over the points in time given by  $t_{\text{avg}}$ . The time-averaged and domain-averaged cloud-top altitudes are given as  $z_{t,\text{avg}}$  in Table 4. In Figure 3b, we show the simulated values of  $E_u + E_v$  and  $E_w$  used for calculation of  $R$  in Figure 3a. To make the figure clear,  $E_w$  has been multiplied by 100 and is represented by the lines predominantly above the black dashed line indicating  $-5/3$  scaling.

We find that the simulations generally agree well with the measurements. The simulated turbulence is nearly isotropic at scales smaller than  $\sim z_{t,\text{avg}}$ , and we see increasing  $R$  for scales larger than  $\sim z_{t,\text{avg}}$ . There are, however, notable differences between the simulations. Focusing on scales resolved at all three

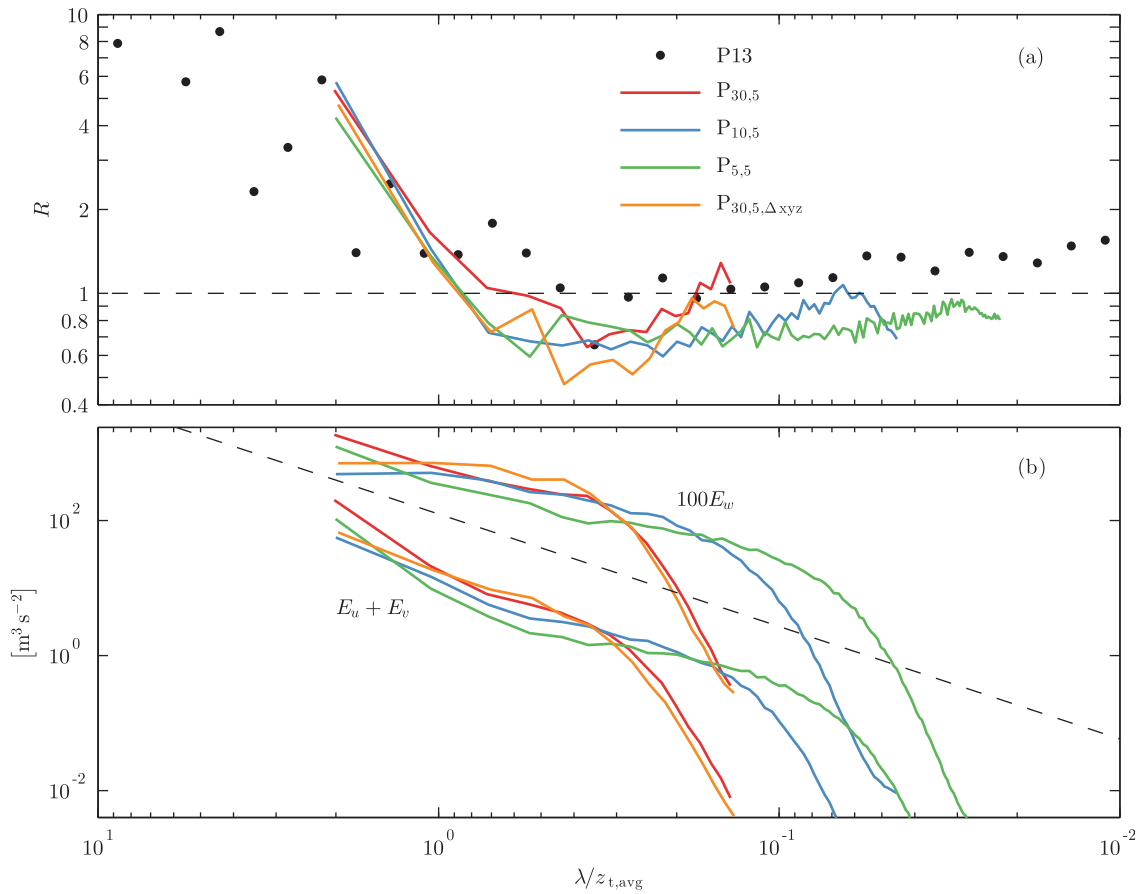


**Figure 3.** Lines and circles represent simulated and measured values of (a)  $R$  and (b)  $E_u + E_v$  and  $E_w$  (multiplied by 100 for clarity) at  $z_{t+}$  (see Table 4). Simulated values are averages over the last 2 h of the simulation period.

horizontal grid spacings (30, 10, and 5 m), we find that simulation  $P_{30,5}$  gives the best agreement with the P13 observations. It captures the change from  $R > 1$  to  $R < 1$  at  $\lambda/z_{t,avg} \simeq 0.35$ , the minimum at  $\lambda/z_{t,avg} \simeq 0.35$ , and the rapid increase in  $R$  for  $\lambda$  larger than  $\sim 0.35z_{t,avg}$ . At the scales resolved in  $P_{30,5}$ ,  $R$ -values from  $P_{10,5}$  and  $P_{5,5}$  are similar. They both capture the observed  $R_{min}$  at  $\lambda \simeq 0.35z_{t,avg}$ , but exhibit nearly constant values of  $R$  in the interval of approximately  $0.1 < \lambda/z_{t,avg} < 0.7$ . Neither of them predict the slight dominance of horizontal fluctuations ( $R > 1$ ) at the smallest scales. We see this as an indication that the vertical grid spacing of 5 m is still too coarse to accurately account for wind shear and vertical temperature gradients in the cloud-top region. Increasing the horizontal grid spacing seems to somewhat counteract this deficiency. As shown by Margolin et al. (2006) for the two-dimensional Navier-Stokes equations, the implicit normal SGS stresses in the  $x$ -direction and  $y$ -direction associated with MPDATA are to the lowest order given by:

$$\tau^{xx} = \left( \frac{1}{4} u_x |u_x| + \frac{1}{12} u_x u_x + \frac{1}{3} u u_{xx} \right)_x \Delta x^2 \quad (13)$$

$$\tau^{yy} = \left( \frac{1}{4} v_y |v_y| + \frac{1}{12} v_y v_y + \frac{1}{3} v v_{yy} \right)_y \Delta y^2, \quad (14)$$

where subscripts  $x$  and  $y$  indicate spatial differentiation in those two directions. Assuming similar relations in the three-dimensional case considered here, the SGS anisotropy

$$R_{SGS} = \frac{\tau^{xx} + \tau^{yy}}{2\tau^{zz}} \quad (15)$$

would, with all other things equal, increase with  $\Delta x$  and  $\Delta y$ . We further hypothesize that such an increase would be reflected in the resolved anisotropy—particularly at scales close to the grid spacing—and that this explains the  $\Delta_{xy}$ -dependency seen in Figure 3.

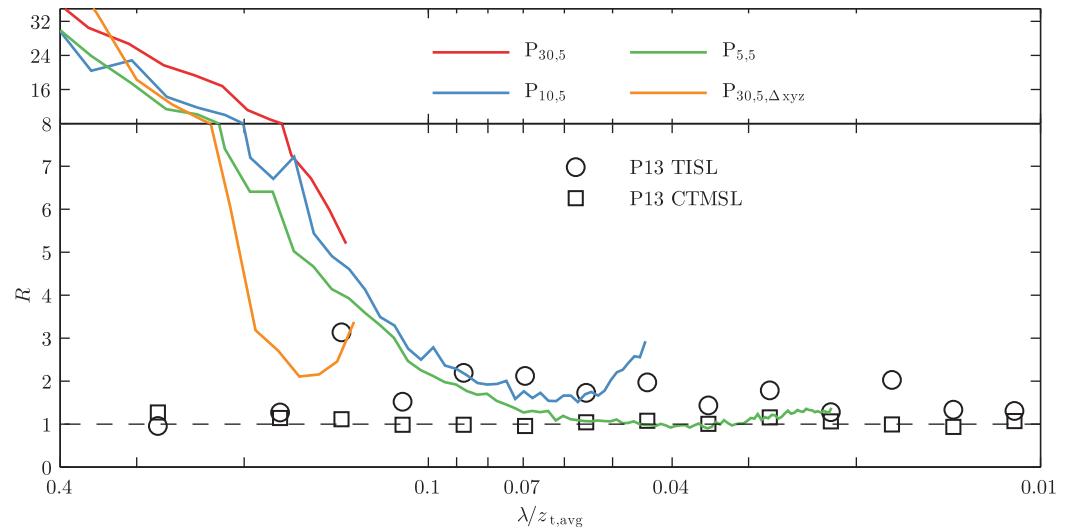


**Figure 4.** Simulated (lines) and observed (circles) values of  $R$  in the TISL. Square markers represent observations in the CTMSL.

The underestimation of  $R$  in  $P_{5,5}$  also occurs in the TISL, as shown in Figure 4. Using the same threshold values as for the measurements ( $\partial\langle\theta_l\rangle/\partial z = 0.2 \text{ K m}^{-1}$  and  $\langle\text{TKE}\rangle = 0.1 \text{ m}^2 \text{ s}^{-2}$ ) we determine the simulated altitude of  $z_{\text{FT/TISL}}$  through vertical interpolation. In both  $P_{30,5}$ ,  $P_{10,5}$ , and  $P_{5,5}$ , we find that the thickness of the TISL ( $\Delta_{\text{TISL}} = z_{\text{FT/TISL}} - \langle z_t \rangle$ ) averaged over  $t_{\text{avg}}$  is approximately 4 m. This is  $\sim 3.5$  times thinner than the observed TISL in P13 and less than the vertical grid spacing.  $\Delta_{\text{TISL}} < \Delta z$  is possible as both  $z_{\text{FT/TISL}}$  and  $z_t$  are determined through vertical interpolation between neighboring vertical grid levels and may differ from multiples of  $\Delta z$ . The lines in Figure 4 represent  $t_{\text{avg}}$ -averages of  $R$  evaluated at the vertical grid levels closest to  $\frac{1}{2}(z_{\text{FT/TISL}} + \langle z_t \rangle)$ , i.e., the middle of the simulated TISL. Circles represent P13 observations averaged across the whole depth of the TISL. At scales smaller than  $\sim 0.08z_{t,\text{avg}}$ , we find that  $P_{5,5}$  predicts nearly isotropic turbulence with  $R \simeq 1$ , while the observations indicate  $R \simeq 2$  (with large variations however).  $P_{10,5}$  only resolves few scales in this range, but seems to agree better with the observations than  $P_{5,5}$ . As at  $z_{t+}$ , we speculate that the vertical grid spacing of 5 m is too coarse to adequately resolve vertical gradients in the TISL, and that the adverse effect of this on  $R$  to some extent can be mitigated by increasing the horizontal grid spacing, i.e., by using anisotropic grid cells. For the few observational data points with  $\lambda/z_{t,\text{avg}} > 0.1$ , all the simulations tend to overestimate  $R$ , especially  $P_{30,5}$ . The square markers in Figure 4 represent observations from the CTMSL. In the simulations, we are not able to clearly identify the interface between the CTMSL and the CTL according to the definition proposed by Malinowski et al. (2013), and we are therefore not able to show simulated  $R$ -values from the CTMSL for comparison with the observations. Supporting information Figure S4 shows  $R$  at all vertical levels between  $0.8z_{t,\text{avg}}$  and  $1.05z_{t,\text{avg}}$  in  $P_{30,5}$ ,  $P_{10,5}$ , and  $P_{5,5}$ .

Regarding the influence of including explicit SGS terms in simulations based on P13, we find that increasing the SGS length scale  $\Delta$  from 0 (ILES) to  $\Delta = (\Delta x \Delta y \Delta z)^{1/3}$  (commonly used in LES) clearly affects  $R$ . Comparing  $P_{30,5}$  and  $P_{30,5,\Delta xyz}$ , we see that moving from ILES to LES leads to a decrease in  $R$  both at  $z_{t+}$  (Figure 3) and in the TISL (Figure 4). The differences become more clear with  $\Delta = \Delta x$  and less clear with  $\Delta = \Delta z$ ; Figures 5a–5d show  $R$  as a function of normalized height and wavelength averaged over the last 2 h of  $P_{30,5}$ ,  $P_{30,5,\Delta z}$ ,  $P_{30,5,\Delta xyz}$ , and  $P_{30,5,\Delta x}$ . Focusing on heights lower than  $z_i$  (indicated by the dash-dotted lines) we see a general tendency of  $R$  to decrease with increasing  $\Delta$ . Note, e.g., the decrease in extent of the dark red area with  $R > 5$  (see also supporting information Figure S5). We presume that this is related to a decrease in inversion strength with increasing  $\Delta$  (see  $\frac{\partial}{\partial z} \langle \theta_l \rangle$  in supporting information Figure S2) allowing for stronger vertical fluctuations.

#### 4.2.2. DYCOMS-II Flight 1 Simulations

To supplement some of the findings based on simulation of P13, we have also performed a series of simulations based on the widely used data from D1 (see Table 2 for an overview). Figure 6 shows  $R$  at  $z = z_{t+}$  (i.e., 100 m below the cloud top, see Table 4) averaged over the last 2 h of the performed D1 simulations (lines). Circles represent observations from  $z_{t+}$ . All three simulations capture the general trends of the observations;

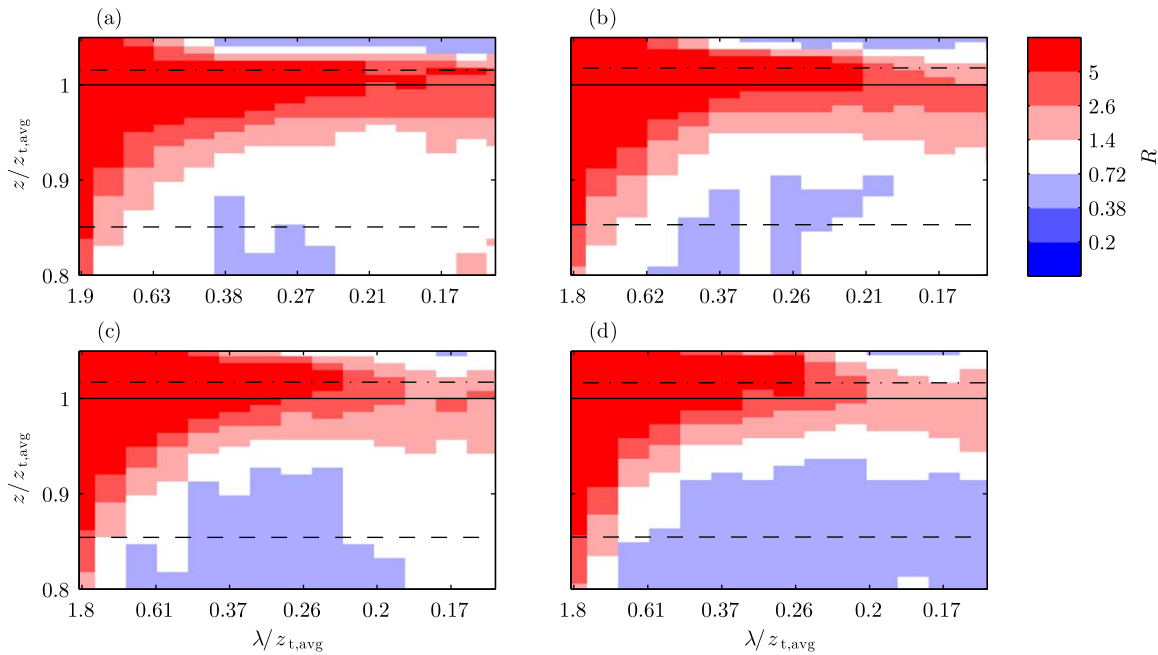


**Figure 5.**  $R$  as a function of normalized height and wavelength averaged over the last 2 h of (a)  $P_{30,5}$ , (b)  $P_{30,5,\Delta z}$ , (c)  $P_{30,5,\Delta xyz}$ , and (d)  $P_{30,5,\Delta xy}$ . Dark red areas represent  $R > 5$  and dark blue areas  $R < 0.2$ . The horizontal lines indicate  $z_{t+}$  (dashed),  $z_{t,avg}$  (solid), and  $z_i$  (dash-dotted, see Figure 1 for the definition of  $z_i$ ). The cloud base is at  $z/z_{t,avg} \approx 0.5$ .

$R$  decreases from values slightly larger than 1 at the smallest scales to a minimum value less than 1 near the middle of the spectrum, after which it increases again to values significantly larger than 1 at the largest scales. The simulated  $R_{min}$ -values are however larger than the observed  $R_{min}$  and occur at smaller scales. At the largest resolved scales, the simulations overestimate  $R$  by a factor of  $\sim 5$ . In contrast to the P13 simulations, we see very little difference between ILES ( $D_{30,5}$ ) and conventional LES ( $D_{30,5,\Delta xyz}$ ) at  $z_{t+}$ , and the impact of decreasing the horizontal grid spacing is also less pronounced. Decreasing  $\Delta_{xy}$  from 30 to 10 m mainly leads to a reduction of  $R$  for  $\lambda < 0.3z_{t,avg}$ . However, as shown in Figure 7, differences between the simulations become more clear at higher altitudes. Especially, we see a clear general reduction in  $R$  between  $z_i$  and  $z_{t+}$  (the dash-dotted and dashed lines) as  $\Delta_{xy}$  is reduced to 10 m (comparing Figures 7a and 7b). The difference between  $D_{30,5}$  and  $D_{30,5,\Delta xyz}$  is most clearly seen just above  $z_{t,avg}$  (the solid horizontal line) where  $R$  is reduced in  $D_{30,5,\Delta xyz}$ .

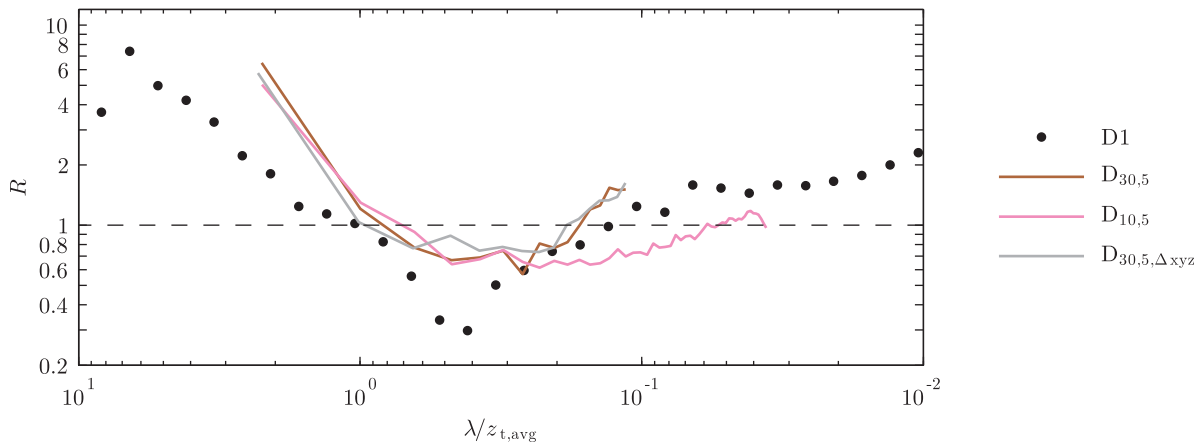


**Figure 6.** Simulated (lines) and measured (circles) values of  $R$  in the DYCOMS-II flight 1 case. Simulated values are averages over the last 2 h of the simulation period.

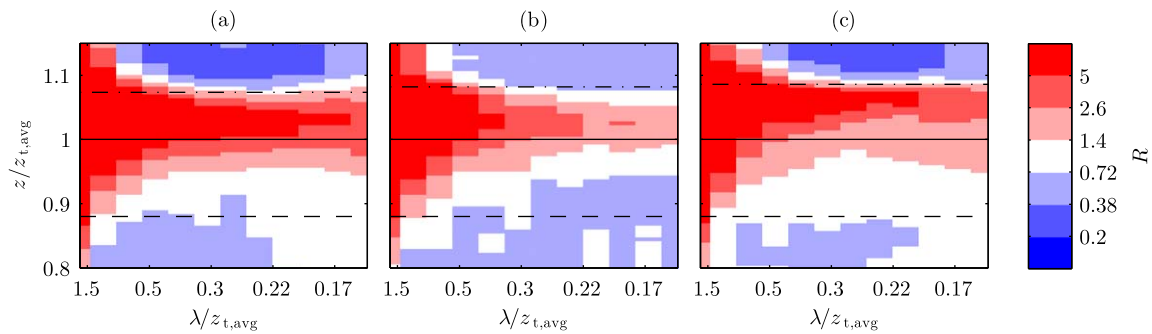


**Figure 7.**  $R$  as a function of height and wavelength averaged over the last 2 h of (a)  $D_{30,5}$ , (b)  $D_{10,5}$ , and (c)  $D_{30,5,\Delta xyz}$ . Dark red areas represent  $R > 5$  and dark blue areas  $R < 0.2$ . The horizontal lines indicate  $z_{t+}$  (dashed),  $z_{t,avg}$  (solid), and  $z_i$  (dash-dotted).

### 4.3. Evolution of the Simulated Cloud

As shown in section 4.2, changes in horizontal grid spacing and SGS mixing length have significant effects on the anisotropy of simulated turbulence in the cloud-top region, and we find it reasonable to assume that such effects in turn also affect entrainment and cloud evolution. Considering a fixed value of  $E_u + E_v$  at a given wavelength, a decrease in  $R$  would mean an increase in  $E_w$  which we intuitively associate with enhanced entrainment, i.e., we expect increased energy of vertical fluctuations to intensify vertical mixing across the STBL top. We see this as the main link between  $R$  and  $w_e$  (see also Kazil et al. (2017) regarding the dependence of entrainment velocity on anisotropy of mesoscale turbulence). On the other hand, with a fixed value of  $E_w$  it is still conceivable that changes in  $R$  (i.e., through changes in  $E_u$  and/or  $E_v$ ) would affect the cloud evolution, e.g., by modulating horizontal mixing across the lateral boundaries of “cloud holes” (i.e., narrow cloud regions with sharply reduced LWC (Gerber et al., 2005)), or by enhancing/weakening cloud-top wind shear and thereby destabilizing/stabilizing the EIL (see, e.g., Katzwinkel et al., 2012; Mellado et al., 2014). Detailed investigation of such phenomena is however beyond the scope of this paper, and here we merely examine the temporal evolution of the domain-averaged LWP in relation to the observed changes in  $R$ .

The LWP is considered an important climatological parameter and  $\langle \text{LWP} \rangle$  is often used as a bulk measure in analysis of results from STBL simulations (e.g., Moeng, 2000; Stevens et al., 2005). Figure 8 shows  $\langle \text{LWP} \rangle$  as a function of time, and we see clear differences between the performed simulations. Decreased horizontal grid spacing and increased SGS mixing length—both associated with increased dominance of vertical fluctuations (decreased  $R$ )—result in lower values of  $\langle \text{LWP} \rangle$ . Averaging over the last 2 h of the simulation

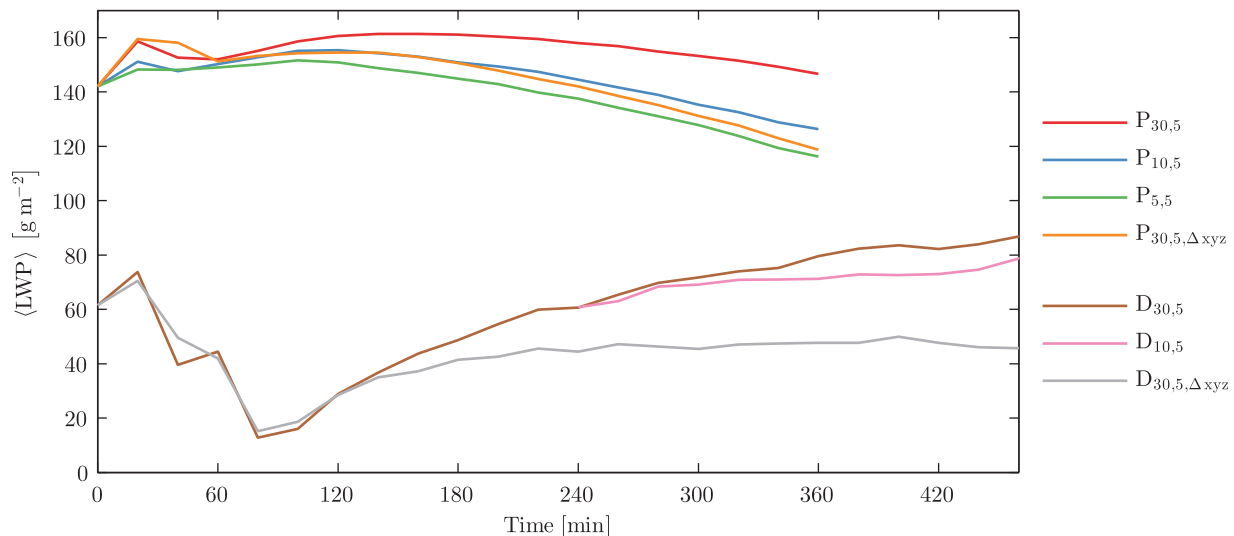


**Figure 8.** Domain-averaged LWP as a function of time.

**Table 5**  
Results From Simulations Based on P13 and D1<sup>a</sup>

	P <sub>5,5</sub>	P <sub>10,5</sub>	P <sub>30,5</sub>	P <sub>30,5,Δz</sub>	P <sub>30,5,Δxyz</sub>	P <sub>30,5,Δx</sub>	D <sub>10,5</sub>	D <sub>30,5</sub>	D <sub>30,5,Δxyz</sub>
$w_e$	6.3	6.3	6.1	7.0	7.5	7.7	1.8	1.1	1.6
$\frac{\partial}{\partial t} \langle \text{LWP} \rangle$	−10.4	−9.2	−5.4	−8.9	−11.3	−12.7	3.0	5.4	−0.7

<sup>a</sup>Simulated entrainment velocities in units of  $\text{mm s}^{-1}$  and  $\frac{\partial}{\partial t} \langle \text{LWP} \rangle$  in units of  $\text{g h}^{-1} \text{m}^{-2}$ . The given values are averages over the last 2 h of the simulations.

period, we obtain the values of  $\frac{\partial}{\partial t} \langle \text{LWP} \rangle$  given in Table 5 which also shows values of simulated entrainment velocities given by

$$w_e = \frac{\partial z_i}{\partial t} + w_s(z_i). \quad (16)$$

In P13 (D1) simulations, we use the uppermost altitude of  $\partial \langle \theta_i \rangle / \partial z = 0.2 \text{ K m}^{-1}$  ( $\partial \langle \theta_i \rangle / \partial z = 0.1 \text{ K m}^{-1}$ ) as a measure of the inversion height  $z_i$ , and calculate temporal derivatives based on data stored at 20 min intervals using central differencing.

As recently shown by van der Dussen et al. (2014, 2016),  $\frac{\partial}{\partial t} \langle \text{LWP} \rangle$  can be seen as the sum of contributions from entrainment, fluxes at the cloud base, divergence of the radiative flux across the cloud layer, precipitation, and large-scale subsidence. Here we will refrain from presenting a full analysis of the contributions to  $\frac{\partial}{\partial t} \langle \text{LWP} \rangle$  and just have a brief look at the correlation between entrainment velocity and LWP-tendency. As seen from the values in Table 5, increased  $w_e$  is typically associated with decreased  $\frac{\partial}{\partial t} \langle \text{LWP} \rangle$ . At this point, however, we cannot say if increased entrainment velocity and subsequently decreased  $\frac{\partial}{\partial t} \langle \text{LWP} \rangle$  is caused by increased/decreased dominance of vertical/horizontal fluctuations in the cloud-top region (decreased  $R$ ), or if the changes in  $R$  and  $w_e$  just happens concurrently due to the changes in simulation setup.

We note that in both the P13 case and the D1 case, the simulated entrainment velocities are smaller than the observed  $w_e$  (see Figure 2). However, regarding P13, Gerber et al. (2013) state that the estimated value of  $27.2 \text{ mm s}^{-1}$  is unrealistically high when comparing to the observed cloud-top rise rate of  $9.3 \text{ mm s}^{-1}$ , and in the D1 simulations we have deliberately not included large-scale subsidence (to avoid excessive cloud thinning) and thereby reduced  $w_e$  in comparison to observations. Assuming  $w_s = 3.75 \times 10^{-6} \text{ m s}^{-1}$  as suggested by Stevens et al. (2005) and simply adding  $w_s(z_i)$  to the values of  $w_e$  given in Table 5, we get  $5.1$ ,  $4.4$ , and  $4.9 \text{ mm s}^{-1}$  in  $D_{10,5}$ ,  $D_{30,5}$ , and  $D_{30,5,\Delta xyz}$ , in reasonable agreement with the observation-based estimate of  $\sim 3.9 \text{ mm s}^{-1}$ . In general, the simulation setups represent very idealized versions of the actual conditions in which the measurements took place. For more realistic results, one should consider including effects of baroclinicity and unsteady forcing (see, e.g., Pedersen et al., 2013); as shown by Kopec et al. (2016) for the P13 case, forced wind shear across the inversion decreases  $\langle \text{LWP} \rangle$ . It is also possible that more detailed modeling of microphysics (e.g., Jarecka et al., 2013; Morrison & Grabowski, 2008) and longwave radiation (Yamaguchi & Randall, 2012) as well as inclusion of precipitation (drizzle) would affect the simulated entrainment rate.

## 5. Summary and Discussion

Observations from seven research flights, representing different types of the STBL (daytime/nocturnal and classical/nonclassical), show clear similarities regarding anisotropy of turbulence at  $z = z_{t+}$  approximately 100 m below the cloud top. The observed turbulence tends to be weakly/strongly dominated by horizontal fluctuations at scales significantly smaller/larger than the cloud-top height. At scales slightly smaller than  $z_{t,\text{avg}}$  we see a dominance of vertical fluctuations. We explain the observed scale-dependency of  $R$  in terms of the Ozmidov and Corrsin scales and the cellular organization of convectively driven large-scale turbulence. In POST flight 13, we furthermore find the observed turbulence in the TISL/CTMSL to be more/less anisotropic (higher/lower values of  $R$ ) than at  $z = z_{t+}$ . This is in agreement with helicopter measurements shown in Katzwinkel et al. (2012, Figure 2), indicating isotropic turbulence in a  $\sim 40 \text{ m}$  thick layer below the cloud top and anisotropic turbulence above and below this layer. In the D1 case, we have no observations



closer to the inversion than those at  $z=z_{t+}$ , and we can unfortunately not say anything about the height-dependence of  $R$ .

In terms of  $R$  at  $z=z_{t+}$ , we find that LES and ILES of the STBL generally agree quite well with observations. There are however notable differences among the performed simulations and between simulations and observations. With the shortest horizontal grid spacing considered here (5 m in the  $P_{5.5}$  ILES of P13), turbulence at scales smaller than  $\sim z_{t,avg}$  is slightly, but consistently and in contrast to the observations, dominated by vertical fluctuations. Similarly in the TISL, we find that  $P_{5.5}$  underestimates  $R$  at the smallest resolved scales when compared to the observations, approximately by a factor of 2. Furthermore, we find that the thickness of the TISL in all P13 simulations is approximately 4 times thinner than the observed TISL. This is most likely caused by excessive radiative cooling in the simulations, acting to maintain a too strong inversion and to force  $z_{FT/TISL}$  and  $z_{TISL/CTMSL}$  too closely together. In the D1 simulations, the radiative cooling is weaker, the inversion less sharp, and the separation between  $z_{FT/TISL}$  and  $z_{TISL/CTMSL}$  larger.

Increasing the horizontal grid spacing in ILES tends to make the simulated turbulence more dominated by horizontal fluctuations and decrease the entrainment velocity. While the impact is quite small in the P13 case (increasing  $\Delta_{xy}$  from 10 to 30 m leads to a decrease in  $w_e$  of  $0.2 \text{ mm s}^{-1} \simeq 0.1 \Delta z/h$ ) it is consistent over time, and we find the impact on the domain-averaged LWP over the full simulation period to be significant. In both P13 simulations and D1 simulations increasing the SGS mixing length from  $\Delta = 0$  to  $\Delta = (\Delta x \Delta y \Delta z)^{1/3}$  (i.e., changing from ILES to conventional LES) tends to predominantly decrease  $R$  and increase the entrainment velocity. In the P13 case, we furthermore find that these effects become less (more) pronounced with  $\Delta = \Delta z$  ( $\Delta = \Delta x$ ). Increased  $w_e$  generally leads to decreased  $\frac{\partial}{\partial t} \langle \text{LWP} \rangle$  and  $\langle \text{LWP} \rangle$ . We argue that the concurrency of increased dominance of horizontal fluctuations and decreased entrainment velocity in the performed simulations supports the suggestion of Jen-La Plante et al. (2016) to revisit entrainment parameterizations with anisotropy of entraining eddies in mind. However, more work is needed to fully establish and understand a potential cause-and-effect relationship between increased  $R$  and decreased  $w_e$ ; especially when considering that the initial analysis of flight data in terms  $R$  presented here, shows no clear correlation between these two parameters.

The analysis presented here along with the findings of Jen-La Plante et al. (2016) and Pedersen et al. (2016) suggests that future LES/ILES studies aimed at improved understanding of the role of anisotropic turbulence in the cloud-top region should focus on its SGS representation. Observations show that cloud-top turbulence is likely to be anisotropic at scales down to a few meters, and turbulence at such small scales is not well-resolved even with a grid spacing of 2.5 m which is considered short in current LES/ILES studies of the STBL. Anisotropy should be accounted for by the applied SGS model or the implicit SGS fluxes in ILES. Some work has been done in this direction; Sullivan et al. (1994) proposed an SGS model including an isotropy factor for more accurate simulation of the atmospheric surface layer, and the SAM simulations (Khairoutdinov & Randall, 2003) in the D1 LES intercomparison study by Stevens et al. (2005) employ an SGS model similar to the one used here but with horizontal eddy diffusivities differing from vertical eddy diffusivities by a factor of  $(\Delta_{xy}/\Delta z)^2$ . More recently, promising results were presented by Matheou and Chung (2014) using the buoyancy-adjusted stretched-vortex SGS model (BASVM; Chung & Matheou, 2014) in LES of the atmospheric boundary layer, and by Montecchia et al. (2017) using the explicit algebraic SGS model (EAM; Marstorp et al., 2009) in LES of high Reynolds number channel flow; both models account for SGS anisotropy. However, as an alternative to introducing still more complex SGS modeling, the possibility of nesting DNS within an LES/ILES domain and thereby reducing the need for advanced SGS modeling, should also be considered (as suggested by Mellado (2017)). A first step in this direction, should be a study of how well anisotropy of small-scale turbulence is represented in existing DNS of stratocumulus clouds (e.g., de Lozar & Mellado, 2015; Mellado et al., 2014).

Here we have suggested the scale-dependent anisotropy measure  $R$  as a metric to supplement more typical measures used in assessment of the fidelity of STBL simulations, such as the ability to reproduce observed inertial-sublayer scaling, vertical profiles of mean quantities, LWP, and cloud cover. In addition, we anticipate, that further analysis of the POST data in terms of  $R$ , including all flights and observations at several altitudes will provide new information about cloud-top turbulence and further facilitate improvement of entrainment parameterizations.

## Acknowledgments

This research was supported by the Polish National Science Centre, grant agreement 2013/08/A/ST10/00291. NCAR is sponsored by the U.S. National Science Foundation. WWG contribution to this work was partially supported by the Polish National Science Center (NCN) "POLONEZ 1" grant 2015/19/P/ST10/02596. The POLONEZ grant has received funding from the European Union's Horizon 2020 Research and Innovation Program under the Marie Skłodowska-Curie Grant Agreement 665778. We would like to acknowledge high-performance computing support from Yellowstone (ark:/85065/d7wd3xhc) provided by NCAR's Computational and Information Systems Laboratory, sponsored by the National Science Foundation, and from the Interdisciplinary Centre for Mathematical and Computational Modelling (ICM) at the University of Warsaw (grant G64-5). The simulation data presented in this paper can be obtained from the corresponding author upon request. Observational data are available from <https://data.eol.ucar.edu/project/POST> and <https://data.eol.ucar.edu/project/DYCOMS-II>. Finally, we would like to thank the two anonymous reviewers for their constructive comments.

## References

- Agee, E. M., Chen, T. S., & Dowell, K. E. (1973). A review of mesoscale cellular convection. *Bulletin of the American Meteorological Society*, 54, 1004–1012. [https://doi.org/10.1175/1520-0477\(1973\)054<1004:AROMCC>2.0.CO;2](https://doi.org/10.1175/1520-0477(1973)054<1004:AROMCC>2.0.CO;2)
- Caughey, S. J., Crease, B. A., & Roach, W. T. (1982). A field study of nocturnal stratocumulus II turbulence structure and entrainment. *Quarterly Journal of the Royal Meteorological Society*, 108, 125–144. <https://doi.org/10.1002/qj.49710845508>
- Cheng, A., Xu, K.-M., & Stevens, B. (2010). Effects of resolution on the simulation of boundary-layer clouds and the partition of kinetic energy to subgrid scales. *Journal of Advances in Modeling Earth Systems*, 2, 3. <https://doi.org/10.3894/JAMES.2010.2.3>
- Chung, D., & Matheou, G. (2014). Large-eddy simulation of stratified turbulence. Part I: A vortex-based subgrid-scale model. *Journal of the Atmospheric Sciences*, 71, 1863–1879. <https://doi.org/10.1175/JAS-D-13-0126.1>
- Clark, T. L., & Farley, R. D. (1984). Severe downslope windstorm calculations in two and three spatial dimensions using anelastic interactive grid nesting: A possible mechanism for gustiness. *Journal of the Atmospheric Sciences*, 41, 329–350. [https://doi.org/10.1175/1520-0469\(1984\)041<0329:SDWCIT>2.0.CO;2](https://doi.org/10.1175/1520-0469(1984)041<0329:SDWCIT>2.0.CO;2)
- Deardorff, J. W. (1980). Stratocumulus-capped mixed layers derived from a three-dimensional model. *Boundary-Layer Meteorology*, 18, 495–527. <https://doi.org/10.1007/BF00119502>
- de Lozar, A., & Mellado, J. P. (2013). Direct numerical simulations of a smoke cloud-top mixing layer as a model for stratocumuli. *Journal of the Atmospheric Sciences*, 70, 2356–2375. <https://doi.org/10.1175/JAS-D-12-0333.1>
- de Lozar, A., & Mellado, J. P. (2015). Mixing driven by radiative and evaporative cooling at the stratocumulus top. *Journal of the Atmospheric Sciences*, 72, 4681–4700. <https://doi.org/10.1175/JAS-D-15-0087.1>
- de Roode, S. R., Duynkerke, P. G., & Jonker, H. J. (2004). Large-eddy simulation: How large is large enough? *Journal of the Atmospheric Sciences*, 61, 403–421. [https://doi.org/10.1175/1520-0469\(2004\)061<0403:LSHLIL>2.0.CO;2](https://doi.org/10.1175/1520-0469(2004)061<0403:LSHLIL>2.0.CO;2)
- Gerber, H., Frick, G., Malinowski, S. P., Brenguier, J.-L., & Burnet, F. (2005). Holes and entrainment in stratocumulus. *Journal of the Atmospheric Sciences*, 62, 443–459. <https://doi.org/10.1175/JAS-3399.1>
- Gerber, H., Frick, G., Malinowski, S. P., Jonsson, H., Khelif, D., & Krueger, S. K. (2013). Entrainment rates and microphysics in POST stratocumulus. *Journal of Geophysical Research*, 118, 12094–12109. <https://doi.org/10.1002/jgrd.50878>
- Gerber, H., Frick, G., Malinowski, S. P., Kumula, W., & Krueger, S. (2010). POST—A new look at stratocumulus. In *13th conference on cloud physics*. Portland, OR: American Meteorological Society.
- Grabowski, W. W. (2014). Extracting microphysical impacts in large-eddy simulations of shallow convection. *Journal of the Atmospheric Sciences*, 71, 4493–4499. <https://doi.org/10.1175/JAS-D-14-0231.1>
- Grabowski, W. W., & Smolarkiewicz, P. K. (1990). Monotone finite-difference approximations to the advection-condensation problem. *Monthly Weather Review*, 118, 2082–2098. [https://doi.org/10.1175/1520-0493\(1990\)118<2082:MFDATT>2.0.CO;2](https://doi.org/10.1175/1520-0493(1990)118<2082:MFDATT>2.0.CO;2)
- Grabowski, W. W., & Smolarkiewicz, P. K. (2002). A multiscale anelastic model for meteorological research. *Monthly Weather Review*, 130, 939–956. [https://doi.org/10.1175/1520-0493\(2002\)130<0939:AMAMFM>2.0.CO;2](https://doi.org/10.1175/1520-0493(2002)130<0939:AMAMFM>2.0.CO;2)
- Grinstein, F. F., Margolin, L. G., & Rider, W. J. (2007). *Implicit large eddy simulation: Computing turbulent fluid dynamics*. New York, NY: Cambridge University Press.
- Guo, H., Liu, Y., Däum, P. H., Senum, G. I., & Tao, W.-K. (2008). Characteristics of vertical velocity in marine stratocumulus: Comparison of large eddy simulations with observations. *Environmental Research Letters*, 3, 045020. <https://doi.org/10.1088/1748-9326/3/4/045020>
- Jarecka, D., Pawłowska, H., Grabowski, W. W., & Wyszogrodzki, A. A. (2013). Modeling microphysical effects of entrainment in clouds observed during EUCAARI-IMPACT field campaign. *Atmospheric Chemistry and Physics*, 13, 8489–8503. <https://doi.org/10.5194/acp-13-8489-2013>
- Jen-La Plante, I., Ma, Y., Nurowska, K., Gerber, H., Khelif, D., Karpinska, K., et al. (2016). Physics of Stratocumulus Top (POST): Turbulence characteristics. *Atmospheric Chemistry and Physics*, 16, 9711–9725. <https://doi.org/10.5194/acp-16-9711-2016>
- Kaimal, J. C., Wyngaard, J. C., Haugen, D. A., Coté, O. R., Izumi, Y., Caughey, S. J., et al. (1976). Turbulence structure in the convective boundary layer. *Journal of the Atmospheric Sciences*, 33, 2152–2169. [https://doi.org/10.1175/1520-0469\(1976\)033<2152:TSITCB>2.0.CO;2](https://doi.org/10.1175/1520-0469(1976)033<2152:TSITCB>2.0.CO;2)
- Katzwinkler, J., Siebert, H., & Shaw, R. A. (2012). Observation of a self-limiting, shear-induced turbulent inversion layer above marine stratocumulus. *Boundary-Layer Meteorology*, 145, 131–143. <https://doi.org/10.1007/s10546-011-9683-4>
- Kazil, J., Yamaguchi, T., & Feingold, G. (2017). Mesoscale organization, entrainment, and the properties of a closed-cell stratocumulus cloud. *Journal of Advances in Modeling Earth Systems*, 9, 2214–2229. <https://doi.org/10.1002/2017MS001072>
- Kelly, M., & Wyngaard, J. C. (2006). Two-dimensional spectra in the atmospheric boundary layer. *Journal of the Atmospheric Sciences*, 63, 3066–3070. <https://doi.org/10.1175/JAS3769.1>
- Khairoutdinov, M. F., & Randall, D. A. (2003). Cloud resolving modeling of the ARM summer 1997 IOP: Model formulation, results, uncertainties, and sensitivities. *Journal of the Atmospheric Sciences*, 60, 607–625. [https://doi.org/10.1175/1520-0469\(2003\)060<0607:CRMOTA>2.0.CO;2](https://doi.org/10.1175/1520-0469(2003)060<0607:CRMOTA>2.0.CO;2)
- Khani, S., & Waite, M. L. (2015). Large eddy simulations of stratified turbulence: The dynamic Smagorinsky model. *Journal of Fluid Mechanics*, 773, 327–344. <https://doi.org/10.1017/jfm.2015.249>
- Kopec, M. K., Malinowski, S. P., & Piotrowski, Z. P. (2016). Effects of wind shear and radiative cooling on the stratocumulus-topped boundary layer. *Quarterly Journal of the Royal Meteorological Society*, 142, 3222–3233. <https://doi.org/10.1002/qj.2903>
- Kurowski, M. J., Grabowski, W. W., & Smolarkiewicz, P. K. (2014). Anelastic and compressible simulation of moist deep convection. *Journal of the Atmospheric Sciences*, 71, 3767–3787. <https://doi.org/10.1175/JAS-D-14-0017.1>
- Kurowski, M. J., Malinowski, S. P., & Grabowski, W. W. (2009). A numerical investigation of entrainment and transport within a stratocumulus-topped boundary layer. *Quarterly Journal of the Royal Meteorological Society*, 135, 77–92. <https://doi.org/10.1002/qj.354>
- Lindborg, E. (2006). The energy cascade in a strongly stratified fluid. *Journal of Fluid Mechanics*, 550, 207–242. <https://doi.org/10.1017/S0022112005008128>
- Malinowski, S. P., Gerber, H., Jen-La Plante, I., Kopec, M. K., Kumala, W., Nurowska, K., et al. (2013). Physics of Stratocumulus Top (POST): Turbulent mixing across capping inversion. *Atmospheric Chemistry and Physics*, 13, 12171–12186. <https://doi.org/10.5194/acp-13-12171-2013>
- Margolin, L. G., & Rider, W. J. (2002). A rationale for implicit turbulence modelling. *International Journal for Numerical Methods in Fluids*, 39, 821–841. <https://doi.org/10.1002/flid.331>
- Margolin, L. G., Rider, W. J., & Grinstein, F. F. (2006). Modeling turbulent flow with implicit LES. *Journal of Turbulence*, 7, N15. <https://doi.org/10.1080/14685240500331595>
- Margolin, L. G., Smolarkiewicz, P. K., & Sorbjan, Z. (1999). Large-eddy simulations of convective boundary layers using nonoscillatory differencing. *Physica D*, 133, 390–397. [https://doi.org/10.1016/S0167-2789\(99\)00083-4](https://doi.org/10.1016/S0167-2789(99)00083-4)

- Marstorp, L., Brethouwer, G., Grundestam, O., & Johansson, A. V. (2009). Explicit algebraic subgrid stress models with application to rotating channel flow. *Journal of Fluid Mechanics*, 639, 403–432. <https://doi.org/10.1017/S0022112009991054>
- Matheou, G., & Chung, D. (2014). Large-eddy simulation of stratified turbulence. Part II: Application of the stretched-vortex model to the atmospheric boundary layer. *Journal of the Atmospheric Sciences*, 71, 4439–4460. <https://doi.org/10.1175/JAS-D-13-0306.1>
- Mauritsen, T., & Svensson, G. (2007). Observations of stably stratified shear-driven atmospheric turbulence at low and high Richardson numbers. *Journal of the Atmospheric Sciences*, 64, 645–655. <https://doi.org/10.1175/JAS3856.1>
- Mellado, J. P. (2010). The evaporatively driven cloud-top mixing layer. *Journal of Fluid Mechanics*, 660, 5–36. <https://doi.org/10.1017/S0022112010002831>
- Mellado, J. P. (2017). Cloud-top entrainment in stratocumulus clouds. *Annual Review of Fluid Mechanics*, 49, 145–169. <https://doi.org/10.1146/annurev-fluid-010816-060231>
- Mellado, J. P., Stevens, B., & Schmidt, H. (2014). Wind shear and buoyancy reversal at the top of stratocumulus. *Journal of the Atmospheric Sciences*, 71, 1040–1057. <https://doi.org/10.1175/JAS-D-13-0189.1>
- Moeng, C.-H. (1986). Large-eddy simulation of a stratus-topped boundary layer. Part I: Structure and budgets. *Journal of the Atmospheric Sciences*, 43, 2886–2900. [https://doi.org/10.1175/1520-0469\(1986\)043<2886:LESOAS>2.0.CO;2](https://doi.org/10.1175/1520-0469(1986)043<2886:LESOAS>2.0.CO;2)
- Moeng, C.-H. (2000). Entrainment rate, cloud fraction, and liquid water path of PBL stratocumulus clouds. *Journal of the Atmospheric Sciences*, 57, 3627–3643. [https://doi.org/10.1175/1520-0469\(2000\)057<3627:ERCFAL>2.0.CO;2](https://doi.org/10.1175/1520-0469(2000)057<3627:ERCFAL>2.0.CO;2)
- Montecchia, M., Brethouwer, G., Johansson, A. V., & Wallin, S. (2017). Taking large-eddy simulation of wall-bounded flows to higher Reynolds numbers by use of anisotropy-resolving subgrid models. *Physical Review Fluids*, 2, 034601. <https://doi.org/10.1103/PhysRevFluids.2.034601>
- Morrison, H., & Grabowski, W. W. (2008). Modeling supersaturation and subgrid-scale mixing with two-moment bulk warm microphysics. *Journal of the Atmospheric Sciences*, 65, 792–812. <https://doi.org/10.1175/2007JAS2374.1>
- Nishizawa, S., Yashiro, H., Sato, Y., Miyamoto, Y., & Tomita, H. (2015). Influence of grid aspect ratio on planetary boundary layer turbulence in large-eddy simulations. *Geoscientific Model Development*, 8, 3393–3419. <https://doi.org/10.5194/gmd-8-3393-2015>
- Noda, A. T., & Satoh, M. (2014). Intermodel variances of subtropical stratocumulus environments simulated in CMIP5 models. *Geophysical Research Letters*, 41, 7754–7761. <https://doi.org/10.1002/2014GL061812>
- Pedersen, J. G., Kelly, M., Gryning, S.-E., & Brümmer, B. (2013). The effect of unsteady and baroclinic forcing on predicted wind profiles in large eddy simulations: Two case studies of the daytime atmospheric boundary layer. *Meteorologische Zeitschrift*, 22, 661–674. <https://doi.org/10.1127/0941-2948/2013/0477>
- Pedersen, J. G., Malinowski, S. P., & Grabowski, W. W. (2016). Resolution and domain-size sensitivity in implicit large-eddy simulation of the stratocumulus-topped boundary layer. *Journal of Advances in Modeling Earth Systems*, 8, 885–903. <https://doi.org/10.1002/2015MS000572>
- Piotrowski, Z. P., Smolarkiewicz, P. K., Malinowski, S. P., & Wyszogrodzki, A. A. (2009). On numerical realizability of thermal convection. *Journal of Computational Physics*, 228, 6268–6290. <https://doi.org/10.1016/j.jcp.2009.05.023>
- Pressel, K. G., Mishra, S., Schneider, T., Kaul, C. M., & Tan, Z. (2017). Numerics and subgrid-scale modeling in large eddy simulations of stratocumulus clouds. *Journal of Advances in Modeling Earth Systems*, 9, 1342–1365. <https://doi.org/10.1002/2016MS000778>
- Prusa, J. M., Smolarkiewicz, P. K., & Wyszogrodzki, A. A. (2008). EULAG, A computational model for multiscale flows. *Computers & Fluids*, 37, 1193–1207. <https://doi.org/10.1016/j.comfluid.2007.12.001>
- Riley, J. J., & Lelong, M.-P. (2000). Fluid motions in the presence of strong stable stratification. *Annual Review of Fluid Mechanics*, 32, 613–657. <https://doi.org/10.1146/annurev.fluid.32.1.613>
- Schmidt, H., & Schumann, U. (1989). Coherent structure of the convective boundary layer derived from large-eddy simulations. *Journal of Fluid Mechanics*, 200, 511–562. <https://doi.org/10.1017/S0022112089000753>
- Scotti, A., Meneveau, C., & Lilly, D. K. (1993). Generalized Smagorinsky model for anisotropic grids. *Physics of Fluids A*, 5, 2306–2308. <https://doi.org/10.1063/1.858537>
- Smolarkiewicz, P. K. (2006). Multidimensional positive definite advection transport algorithm: An overview. *International Journal for Numerical Methods in Fluids*, 50, 1123–1144. <https://doi.org/10.1002/fld.1071>
- Smyth, W. D., & Moum, J. N. (2000). Length scales of turbulence in stably stratified mixing layers. *Physics of Fluids*, 12, 1327–1342. <https://doi.org/10.1063/1.870385>
- Sorbjan, Z. (1996). Numerical study of penetrative and “solid lid” nonpenetrative convective boundary layers. *Journal of the Atmospheric Sciences*, 53, 101–112. [https://doi.org/10.1175/1520-0469\(1996\)053<0101:NSOPAL>2.0.CO;2](https://doi.org/10.1175/1520-0469(1996)053<0101:NSOPAL>2.0.CO;2)
- Stevens, B., Lenschow, D. H., Faloona, I., Moeng, C.-H., Lilly, D. K., Blomquist, B., et al. (2003b). On entrainment rates in nocturnal marine stratocumulus. *Quarterly Journal of the Royal Meteorological Society*, 129, 3469–3493. <https://doi.org/10.1256/qj.02.202>
- Stevens, B., Lenschow, D. H., Vali, G., Gerber, H., Bandy, A., Blomquist, B., et al. (2003a). Dynamics and chemistry of marine stratocumulus—DYCOMS-II. *Bulletin of the American Meteorological Society*, 84, 579–593. <https://doi.org/10.1175/BAMS-84-5-579>
- Stevens, B., Moeng, C.-H., Ackerman, A. S., Bretherton, C. S., Chlond, A., de Roode, S., et al. (2005). Evaluation of large-eddy simulations via observations of nocturnal marine stratocumulus. *Monthly Weather Review*, 133, 1443–1462. <https://doi.org/10.1175/MWR2930.1>
- Sullivan, P. P., McWilliams, J. C., & Moeng, C.-H. (1994). A subgrid-scale model for large-eddy simulation of planetary boundary-layer flows. *Boundary-Layer Meteorology*, 71, 247–276. <https://doi.org/10.1007/BF00713741>
- Sullivan, P. P., Weil, J. C., Patton, E. G., Jonker, H. J., & Mironov, D. V. (2016). Turbulent winds and temperature fronts in large-eddy simulations of the stable atmospheric boundary layer. *Journal of the Atmospheric Sciences*, 73, 1815–1840. <https://doi.org/10.1175/JAS-D-15-0339.1>
- van der Dussen, J. J., de Roode, S. R., & Siebesma, A. P. (2014). Factors controlling rapid stratocumulus cloud thinning. *Journal of the Atmospheric Sciences*, 71, 655–664. <https://doi.org/10.1175/JAS-D-13-0114.1>
- van der Dussen, J. J., de Roode, S. R., & Siebesma, A. P. (2016). How large-scale subsidence affects stratocumulus transitions. *Atmospheric Chemistry and Physics*, 16, 691–701. <https://doi.org/10.5194/acp-16-691-2016>
- Waite, M. L. (2011). Stratified turbulence at the buoyancy scale. *Physics of Fluids*, 23, 066602. <https://doi.org/10.1063/1.3599699>
- Wood, R. (2012). Stratocumulus clouds. *Monthly Weather Review*, 140, 2373–2423. <https://doi.org/10.1175/MWR-D-11-00121.1>
- Wood, R., & Hartmann, D. L. (2006). Spatial variability of liquid water path in marine low cloud: The importance of mesoscale cellular convection. *Journal of Climate*, 19, 1748–1764. <https://doi.org/10.1175/JCLI3702.1>
- Yamaguchi, T., Brewer, W. A., & Feingold, G. (2013). Evaluation of modeled stratocumulus-capped boundary layer turbulence with ship-borne data. *Journal of the Atmospheric Sciences*, 70, 3895–3919. <https://doi.org/10.1175/JAS-D-13-050.1>
- Yamaguchi, T., & Randall, D. A. (2012). Cooling of entrained parcels in a large-eddy simulation. *Journal of the Atmospheric Sciences*, 69, 1118–1136. <https://doi.org/10.1175/JAS-D-11-080.1>